



Lattice field theory simulations of graphene

Joaquín E. Drut¹ and Timo A. Lähde²

¹*Department of Physics, The Ohio State University, Columbus, Ohio 43210-1117, USA*

²*Department of Physics, University of Washington, Seattle, Washington, 98195-1560, USA*

(Received 12 January 2009; revised manuscript received 26 February 2009; published 20 April 2009)

We discuss the Monte Carlo method of simulating lattice field theories as a means of studying the low-energy effective theory of graphene. We also report on simulational results obtained using the Metropolis and Hybrid Monte Carlo methods for the chiral condensate, which is the order parameter for the semimetal-insulator transition in graphene, induced by the Coulomb interaction between the massless electronic quasiparticles. The critical coupling and the associated exponents of this transition are determined by means of the logarithmic derivative of the chiral condensate and an equation-of-state analysis. A thorough discussion of finite-size effects is given, along with several tests of our calculational framework. These results strengthen the case for an insulating phase in suspended graphene, and indicate that the semimetal-insulator transition is likely to be of second order, though exhibiting neither classical critical exponents, nor the predicted phenomenon of Miransky scaling.

DOI: [10.1103/PhysRevB.79.165425](https://doi.org/10.1103/PhysRevB.79.165425)

PACS number(s): 73.63.Bd, 71.30.+h, 05.10.Ln

I. INTRODUCTION

The recent experimental isolation of single atomic layers of graphite, known as graphene, has provided physicists with a novel opportunity to study a strongly coupled system with remarkable many-body and electronic properties, which at the same time can be easily manipulated experimentally.^{1,2} Even more recently, the advent of experiments utilizing samples of suspended graphene, free from the interference of an underlying substrate,³ has provided unprecedented insight into the intrinsic properties of graphene. Among other remarkable discoveries, suspended graphene has been shown to possess a very high carrier mobility even at room temperature, as well as a markedly nonmetallic behavior of the conductivity at low temperatures.

A central property of graphene is that the low-energy electronic spectrum can be described in terms of two flavors of massless, four-component fermionic quasiparticles with linear dispersion.⁴ Indeed, due to the hexagonal honeycomb arrangement of the carbon atoms in the graphene lattice, the band structure of graphene exhibits two inequivalent (but degenerate) “Dirac cones” where the conduction and valence bands touch, as illustrated in Fig. 1(a). Since the energy-momentum relation around a Dirac point is linear as in relativistic theories, the low-energy description of graphene bears a certain resemblance to massless quantum electrodynamics (QED). Nevertheless, an important difference is that the Fermi velocity of the quasiparticles in graphene is as low as $v \approx c/300$, whereby the electromagnetic interaction is rendered essentially instantaneous.

Such a description is well known to account for the physics of graphene on a substrate, where the system exhibits semimetallic properties due to the absence of a gap in the electronic spectrum. While suspended graphene has recently come under intense experimental investigation,³ its spectrum is yet to be computed in a controlled fashion. From the theoretical perspective, the challenging feature of suspended graphene lies in the fact that the Coulomb interaction between the quasiparticles is unscreened which, in conjunction

with the small Fermi velocity, results in a graphene analog of the fine-structure constant $\alpha_g \gtrsim 1$. At such strong coupling, a dynamical transition into a phase fundamentally different from the weakly coupled semimetallic phase of graphene is a strong possibility. In graphene sheets deposited on a substrate, such a transition is effectively inhibited due to the screening of the Coulomb interaction by the dielectric.

Our recent work in Ref. 5 has demonstrated that graphene is expected to undergo a semimetal-insulator transition when the substrate is removed. More specifically, evidence was found that the low-energy effective theory of graphene undergoes a phase transition involving spontaneous chiral symmetry breaking, which takes place at a critical coupling of $\beta_c = 0.072 \pm 0.005$, and within the accuracy of that work the transition appeared to be consistent with classical mean-field exponents. The results reported in Ref. 5 are based on the numerical Monte Carlo simulation of a discretized lattice formulation of the low-energy effective theory of graphene, and the calculation of the chiral condensate, which is the order parameter for excitonic gap formation. In one possible

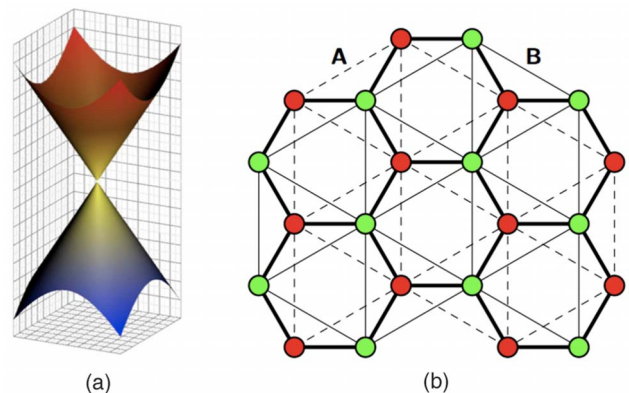


FIG. 1. (Color online) (a) Dirac cone, joining the upper (red) conduction band and the lower (blue) valence band. (b) The hexagonal arrangement of carbon atoms in graphene, with sublattices A (red dots, thin dashed lines) and B (green dots, thin solid lines).

realization of such an insulating state, the equivalence of the triangular sublattices A and B, shown in Fig. 1(b), is broken by the accumulation of charge carriers of opposite sign on the respective sublattices.

Our results should be compared with those of Refs. 6 and 7 which are based on a gap equation, where a semimetal-insulator transition was found at critical couplings of $\beta_c \sim 0.06$ and $\beta_c \sim 0.03$, respectively. While the result of Ref. 6 is within the physical range of Coulomb couplings, that of Ref. 7 is slightly above the largest conceivable value of $\alpha_g \sim 2.16$, which corresponds to graphene in vacuum. On the other hand, Refs. 8 and 9 employed an expansion in the inverse number of fermion flavors N_f , and found that at large N_f , the Coulomb interaction between the quasiparticles becomes irrelevant and therefore unable to induce a gap in the electronic spectrum.

In this paper, we explain the details of our lattice Monte Carlo method, which to our knowledge has not been applied to the low-energy theory of graphene (however, Ref. 10 has considered a theory related to the strong-coupling limit). We also present new calculations supporting the conclusions of Ref. 5, but extending the previous data set to much larger lattices. In Sec. II, we discuss the low-energy effective theory of graphene, the corresponding partition function, and the computation of observables upon integration of the fermionic degrees of freedom. In Sec. III, we describe the discretization of the effective theory and discuss a lattice formulation that respects gauge invariance and avoids the fermion doubling problem while maintaining a certain degree of chiral symmetry at finite lattice spacing. In Sec. V, the results of our simulations are presented, with emphasis on the chiral condensate and susceptibility, including a determination of the critical coupling for the semimetal-insulator phase transition, and the consequences of our results for the corresponding critical exponents. In Sec. VI, we outline the various tests and cross-checks we have performed in order to validate our results. In Sec. VII we discuss the possibility of observing the transition experimentally. Finally, in Sec. VIII we summarize our findings and present a case for continued study.

II. LOW-ENERGY EFFECTIVE THEORY

The electronic band structure of graphene close to the Fermi level forms the basis of the low-energy effective theory of graphene. This band structure is a reflection of the hexagonal arrangement of the carbon atoms as shown in Fig. 1(b), and can be well described by a tight-binding model of the form

$$H = -t \sum_{\langle i,j \rangle, \sigma=\uparrow, \downarrow} (a_{\sigma,i}^\dagger b_{\sigma,j} + \text{H.c.}) - t' \sum_{\langle\langle i,j \rangle\rangle, \sigma=\uparrow, \downarrow} (a_{\sigma,i}^\dagger a_{\sigma,j} + b_{\sigma,i}^\dagger b_{\sigma,j} + \text{H.c.}), \quad (2.1)$$

as first done by Wallace in Ref. 11. The operators $a_{\sigma,i}^\dagger (a_{\sigma,i})$ and $b_{\sigma,i}^\dagger (b_{\sigma,i})$ create (annihilate) an electron of spin σ at location i on the A and B sublattices, respectively [see Fig. 1(b)]. The first term (involving t) takes into account

nearest-neighbor interactions, and the second term (involving t') the next-to-nearest-neighbor ones. Both terms account for all spin states. The hopping parameters that give an optimal fit to the experimentally determined band structure of graphene are $t \approx 2.8$ eV and $t' \approx 0.1$ eV.¹² Third-nearest neighbors have also been considered in Ref. 12, yielding an additional hopping amplitude of $t'' \approx 0.07$ eV.

We shall follow a somewhat different route based on an effective field theory (EFT) treatment of graphene,^{9,13} which has the advantage of describing the physics of graphene directly in terms of the relevant low-energy degrees of freedom, namely, charged massless fermionic quasiparticles. The EFT description of graphene has an additional advantage as it allows for the direct study of effects due to the unscreened, long-range Coulomb interactions between the quasiparticles. In what follows, we shall formulate a *continuum* Lagrangian field theory that should be thought of as valid only at low momenta, much smaller than the inverse of the interatomic distance in graphene, which is ~ 1.42 Å.

A. Continuum formulation

In the EFT framework, graphene is described by a theory of N_f Dirac flavors interacting via an instantaneous Coulomb interaction. The action (in Euclidean space time) of this theory is

$$S_E = - \sum_{a=1}^{N_f} \int d^2x dt \bar{\psi}_a D[A_0] \psi_a + \frac{1}{2g^2} \int d^3x dt (\partial_t A_0)^2, \quad (2.2)$$

where $N_f=2$ for graphene monolayers, $g^2 = e^2 / \epsilon_0$ for graphene in vacuum (suspended graphene), ψ_a is a four-component Dirac field in 2+1 dimensions, A_0 is a Coulomb field in 3+1 dimensions, and

$$D[A_0] = \gamma_0 (\partial_0 + iA_0) + v \gamma_i \partial_i, \quad i = 1, 2, \quad (2.3)$$

where the Dirac matrices γ_μ satisfy the Euclidean Clifford algebra $\{\gamma_\mu, \gamma_\nu\} = 2\delta_{\mu\nu}$. The four-component spinor structure accounts for quasiparticle excitations of sublattices A and B around the two Dirac points in the band structure.^{4,9} The two Dirac points are identified with the two inequivalent representations (with opposite parity) of the Dirac matrices in 2+1 dimensions. In graphene monolayers, $N_f=2$ owing to electronic spin, while $N_f=4$ is related to the case of two decoupled graphene layers, interacting solely via the Coulomb interaction. Consideration of arbitrary N_f is also useful, given that an analytic treatment⁸ is possible in the limit $N_f \rightarrow \infty$.

The strength of the Coulomb interaction is controlled by $\alpha_g = e^2 / (4\pi v \epsilon_0)$, which is the graphene analog of the fine-structure constant $\alpha \approx 1/137$ of QED. It is straightforward to show that α_g is the only parameter, by rescaling according to

$$t' = vt, \quad A'_0 = A_0/v. \quad (2.4)$$

The action (2.2) is invariant under spatially uniform gauge transformations (see Sec. III A). Notice that since the A_0 field

is 3+1 dimensional, one recovers the four-fermion Coulomb interaction

$$\frac{\bar{\psi}_a(x)\gamma_0\psi_a(x)\bar{\psi}_b(x')\gamma_0\psi_b(x')}{|\mathbf{x}-\mathbf{x}'|}, \quad (2.5)$$

by integrating out A_0 . Nevertheless, for our purposes the original form of the action (quadratic in the fermions) as given in Eq. (2.2) is preferable.

A central property of the low-energy EFT is that Eq. (2.2) respects a global $U(2N_f)$ chiral symmetry under the transformations

$$\psi_a \rightarrow \exp(i\Gamma_j\alpha_j)\psi_a, \quad (2.6)$$

where the matrices Γ_j are the $(2N_f)^2$ Hermitian generators of $U(2N_f)$, such that for the case of graphene monolayers, the group is $U(4)$. The generators can be constructed by first choosing a representation for the γ_μ , such as

$$\gamma_0 = \begin{pmatrix} \sigma_3 & 0 \\ 0 & -\sigma_3 \end{pmatrix}, \quad \gamma_i = \begin{pmatrix} \sigma_i & 0 \\ 0 & -\sigma_i \end{pmatrix}, \quad (2.7)$$

where the σ_i are Pauli matrices. Adding the identity to this set yields the generators of $U(2)$, since they form a set of four linearly independent Hermitian matrices. It should be noted that the choice of any particular representation for the γ_μ is completely arbitrary and is not necessary for any calculational purpose, as all relevant information is provided by the Clifford algebra. However, the identification of the spinor degrees of freedom with any particular Dirac point and graphene sublattice is dependent on the chosen representation.

In order to arrive at the generators of $U(4)$, one can take the direct product of each of the above mentioned generators of $U(2)$ by $\{1, \sigma^1, \sigma^2, \sigma^3\}$, where the latter operate in flavor space. In this way, one obtains a set of precisely sixteen linearly independent Hermitian matrices, forming the generators of $U(4)$. Significantly, this chiral symmetry can be spontaneously broken down to $U(2) \times U(2)$, in which case the excitonic condensate $\langle \bar{\psi}\psi \rangle$ acquires a nonvanishing value, signaling the formation of quasiparticle-hole bound states. The same group structure is obtained by adding to Eq. (2.2) a parity invariant (Dirac) mass term

$$\int d^2x dt m_0 \bar{\psi}_a \psi_a, \quad (2.8)$$

which breaks chiral symmetry explicitly. The remaining unbroken generators are then $\{1, \sigma^3\}$, which correspond to uniform phase rotations of both flavors with the same phase, and with equal and opposite phases, respectively. For the extended theory with N_f flavors, the symmetry-breaking pattern is $U(2N_f) \rightarrow U(N_f) \times U(N_f)$.

Other symmetry-breaking patterns, particularly involving the possibility of magnetic as well as Cooper-type pairing instabilities, have been investigated in Refs. 9 and 14.

B. Effective action and probability measure

The partition function corresponding to Eq. (2.2) is given by

$$\mathcal{Z} = \int \mathcal{D}A_0 \mathcal{D}\psi \mathcal{D}\bar{\psi} \exp(-S_E[\bar{\psi}, \psi, A_0]), \quad (2.9)$$

where it is possible to integrate out the fermionic degrees of freedom, as S_E is quadratic in the ψ_a . We thus obtain

$$\mathcal{Z} = \int \mathcal{D}A_0 \exp(-S_E^g[A_0]) \det(D[A_0])^{N_f}, \quad (2.10)$$

where

$$S_E^g = \frac{1}{2g^2} \int d^3x dt (\partial_t A_0)^2 \quad (2.11)$$

is the pure gauge part of the action. It is of central importance for the convergence of the Monte Carlo algorithm that the above determinant has a definite sign, independently of any particular configuration of the gauge field A_0 . One way to prove that this property is satisfied is to choose a specific representation of the Dirac matrices, such as Eq. (2.7), in terms of which $D[A_0]$ can be written as

$$D[A_0] = \begin{pmatrix} M[A_0] & 0 \\ 0 & -M[A_0] \end{pmatrix} = \begin{pmatrix} M[A_0] & 0 \\ 0 & M^\dagger[A_0] \end{pmatrix}, \quad (2.12)$$

where

$$M[A_0] = \sigma_0(\partial_0 + iA_0) + v\sigma_i\partial_i, \quad i = 1, 2, \quad (2.13)$$

and use the facts that A_0 is real, and that the Pauli matrices and the momentum operator are Hermitian. The latter implies $\partial_\mu^\dagger = -\partial_\mu$, and therefore

$$\det(D) = \det(M)\det(M^\dagger) = |\det(M)|^2 > 0, \quad (2.14)$$

which, furthermore, is not affected by the introduction of a parity invariant-mass term such as Eq. (2.8). However, the positivity of $\det(D)$ breaks down in the presence of a chemical potential, which can be thought of as a uniform, imaginary contribution to the A_0 field.

The fact that $\det(D)$ is positive definite allows for the definition of an effective gauge action that is purely real, given by

$$S_{\text{eff}}[A_0] = -N_f \ln \det(D[A_0]) + S_E^g[A_0], \quad (2.15)$$

so that the partition function becomes

$$\mathcal{Z} = \int \mathcal{D}A_0 \exp(-S_{\text{eff}}[A_0]), \quad (2.16)$$

where $P[A_0] = \exp(-S_{\text{eff}}[A_0]) > 0$ can be interpreted as a positive-definite probability measure for a Monte Carlo calculation, as outlined in Sec. III.

C. Operator expectation values

The expectation value of a given operator $O[\bar{\psi}, \psi]$ dependent on the fermion fields can be calculated by taking functional derivatives of the generating functional,

$$\mathcal{Z}[\bar{\eta}, \eta] = \int \mathcal{D}A_0 \mathcal{D}\psi \mathcal{D}\bar{\psi} \exp(-S_E[A_0, \bar{\psi}, \psi, \bar{\eta}, \eta]), \quad (2.17)$$

where source terms have been added to the original action according to

$$S_E[A_0, \bar{\psi}, \psi, \bar{\eta}, \eta] = S_E[A_0, \bar{\psi}, \psi] + \int d^2x dt (\bar{\psi} \eta + \text{H.c.}), \quad (2.18)$$

such that the modified effective gauge action is a functional of A_0 as well as of the sources $\eta, \bar{\eta}$. It is again possible to integrate out the fermionic degrees of freedom and take functional derivatives with respect to the sources in the resulting expression,

$$\mathcal{Z}[\bar{\eta}, \eta] \propto \int \mathcal{D}A_0 \exp(-S_{\text{eff}}[A_0]) \times \exp\left(-\int d^2x dt \bar{\eta} D^{-1}[A_0] \eta\right), \quad (2.19)$$

which makes it possible to obtain expectation values in terms of a path integral over A_0 only. While this procedure is completely general, it is possible to employ a slightly different approach in order to facilitate the computation of the chiral condensate and susceptibility.

The chiral condensate σ , which is the order parameter of the semimetal-insulator phase transition in graphene, is defined by

$$\sigma \equiv \langle \bar{\psi}_b \psi_b \rangle, \quad (2.20)$$

where the fermion fields are evaluated at the same space-time point. It is useful to note that the mass m_0 plays the role of a source, coupled to $\bar{\psi}_b \psi_b$. The expectation value of this operator can therefore be obtained by first differentiating the partition function with respect to m_0 and dividing by the volume, giving

$$\sigma = \frac{1}{V\mathcal{Z}} \int \mathcal{D}A_0 \mathcal{D}\psi \mathcal{D}\bar{\psi} \int dx \bar{\psi}_b(x) \psi_b(x) \exp(-S_E) = \frac{1}{V} \frac{\partial \ln \mathcal{Z}}{\partial m_0}, \quad (2.21)$$

where we have used the fact that space is homogeneous and therefore the volume average of $\bar{\psi}_b(x) \psi_b(x)$ can be replaced by its value at an arbitrary point x . On the other hand, once the fermions have been integrated out, the derivative with respect to m_0 yields

$$\sigma = \frac{1}{V\mathcal{Z}} \int \mathcal{D}A_0 \text{Tr}(D^{-1}[A_0]) \exp(-S_{\text{eff}}[A_0]) = \frac{1}{V} \langle \text{Tr}(D^{-1}[A_0]) \rangle, \quad (2.22)$$

where the identities

$$\det[D(\lambda)] = \exp \text{Tr}[\log[D(\lambda)]], \quad (2.23)$$

$$\frac{\partial \det(D[\lambda])}{\partial \lambda} = \det(D[\lambda]) \text{Tr}\left(D^{-1}[\lambda] \frac{\partial D}{\partial \lambda}\right) \quad (2.24)$$

have been used. The chiral susceptibility χ_l may be found by taking one more derivative with respect to m_0 , giving

$$\chi_l \equiv \frac{\partial \sigma}{\partial m_0} = \frac{1}{V} [\langle \text{Tr}^2(D^{-1}) \rangle - \langle \text{Tr}(D^{-2}) \rangle - \langle \text{Tr}(D^{-1}) \rangle^2], \quad (2.25)$$

which is expected to diverge at a second-order phase transition, and may also yield constraining information on the universal critical exponents of the transition.

III. GRAPHENE ON THE LATTICE

In this section we formulate the lattice version of Eq. (2.2). We begin by discretizing the pure gauge sector, where the requirement of gauge invariance implies the use of “link variables” to represent the gauge degrees of freedom. The “staggered” discretization of the fermionic sector is then outlined, as it is the preferred choice to represent fermions with chiral symmetry at finite lattice spacing.

A. Gauge invariance and link variables

Recall that the pure gauge part of the Euclidean action is given by

$$S_E^g = \frac{1}{2g^2} \int d^3x dt (\partial_t A_0)^2, \quad (3.1)$$

which can be thought of as the nonrelativistic limit of the Lorentz-invariant form $\frac{1}{4} F_{\mu\nu} F^{\mu\nu}$ where $F_{\mu\nu} = \partial_\mu A_\nu - \partial_\nu A_\mu$, such that

$$F_{\mu\nu} F^{\mu\nu} = F_{0j} F^{0j} + F_{ij} F^{ij} + F_{i0} F^{i0} = 2F_{0j} F^{0j} = 2(\partial_j A_0)^2, \quad (3.2)$$

where we have used $F_{ij}=0$ (no magnetic field) and $\partial_0 A_j=0$ (no electric field induction by a magnetic field), valid in the nonrelativistic limit ($v \ll c$). Thus, for graphene the only non-vanishing contribution is the electric field $E_j = -\partial_j A_0$, which represents the instantaneous Coulomb interaction between the quasiparticles.

The action (3.1) is invariant under the time dependent, spatially uniform gauge transformations

$$A_0 \rightarrow A_0 + \alpha(t),$$

$$\psi \rightarrow \exp\left\{i \int_0^t dt' \alpha(t')\right\} \psi, \quad (3.3)$$

where $\alpha(t)$ is a function of time only. Thus, in spite of its apparent simplicity, the effective theory of graphene possesses a truly local gauge invariance, which should be respected by the lattice action. To this end, one introduces temporal link variables

$$U_{0,\mathbf{n}} = U_{\mathbf{n}} \equiv \exp(i\theta_{\mathbf{n}}), \quad (3.4)$$

where $\theta_{\mathbf{n}}$ is the dimensionless lattice gauge field evaluated at the lattice point $\mathbf{n}=(n_0, n_1, n_2, n_3)$. The spatial link variables

$$U_{i,\mathbf{n}} = 1, \quad (3.5)$$

are set to unity. It is convenient to express the discretized version of Eq. (3.1) in terms of “plaquette” variables, defined by

$$U_{\mu\nu,\mathbf{n}} = U_{\mu,\mathbf{n}} U_{\nu,\mathbf{n}+\mathbf{e}_\mu} U_{\mu,\mathbf{n}+\mathbf{e}_\nu}^\dagger U_{\nu,\mathbf{n}}^\dagger, \quad (3.6)$$

where, in the present case of a pure Coulomb interaction, the only nontrivial components are U_{0i} and U_{i0} . Those plaquette components then correspond to the discretized formulation of the electric field. The remaining components corresponding to the magnetic field are equal to unity. These statements can be summarized in the expression

$$U_{\mu\nu,\mathbf{n}} = \delta_{\mu 0} \delta_{\nu i} U_{\mathbf{n}} U_{\mathbf{n}+\mathbf{e}_i}^\dagger + \delta_{\nu 0} \delta_{\mu i} U_{\mathbf{n}}^\dagger U_{\mathbf{n}+\mathbf{e}_i} + \delta_{\mu 0} \delta_{\nu 0} + \delta_{\mu i} \delta_{\nu j}. \quad (3.7)$$

In terms of the gauge link variables and plaquettes, the discretized gauge action corresponding to Eq. (3.1) is given by¹⁵

$$S_E^g = \beta \sum_{\mathbf{n}} \sum_{\mu > \nu} \left[1 - \frac{1}{2} (U_{\mu\nu,\mathbf{n}} + U_{\mu\nu,\mathbf{n}}^\dagger) \right], \quad (3.8)$$

where $\beta = 1/g^2$, such that $\beta \rightarrow v/g^2$ when the rescaling of Eq. (2.4) is applied. In Eq. (3.8), the only nonvanishing contributions arise from the terms with $(\mu, \nu) = (1, 0), (2, 0), (3, 0), (2, 1), (3, 1),$ and $(3, 2)$. Equation (3.8) may be simplified to

$$S_{E,C}^g = \beta \sum_{\mathbf{n}} \left[3 - \sum_{i=1}^3 \Re(U_{\mathbf{n}} U_{\mathbf{n}+\mathbf{e}_i}^\dagger) \right], \quad (3.9)$$

where $\Re(x)$ denotes the real part of x . Equation (3.9) is referred to as the compact formulation of the discretized gauge action. This formulation is known¹⁶ to be suboptimal, as compared to the noncompact formulation, for lattice simulations of QED and related theories. However, the noncompact formulation may be obtained from Eq. (3.9) by expanding $\Re(U_{\mathbf{n}} U_{\mathbf{n}+\mathbf{e}_i}^\dagger)$ to second order in θ ,

$$\Re(U_{\mathbf{n}} U_{\mathbf{n}+\mathbf{e}_i}^\dagger) = 1 - \frac{1}{2} (\theta_{\mathbf{n}+\mathbf{e}_i} - \theta_{\mathbf{n}})^2 + \dots, \quad (3.10)$$

whereupon the noncompact lattice gauge action is given by

$$S_{E,N}^g = \frac{\beta}{2} \sum_{\mathbf{n}} \sum_{i=1}^3 (\theta_{\mathbf{n}+\mathbf{e}_i} - \theta_{\mathbf{n}})^2. \quad (3.11)$$

Here, and throughout the rest of this paper, we have set the lattice spacing to equal unity, and it is thus dropped from all expressions. All dimensionful quantities should therefore be regarded as expressed in units of the lattice spacing.

B. Staggered fermions

While the discretization of the gauge sector is relatively straightforward, the inclusion of dynamical fermions on the lattice is a notoriously difficult problem. One of the main issues when simulating fermions on the lattice is the so-

called doubling problem (for an overview, see Ref. 15, Chapter 4). This problem is related to the chiral invariance of the fermionic sector, and arises due to the appearance of multiple (unwanted) zeros in the inverse propagator. In other words, one is simulating more fermion flavors than expected, the exact number being dependent on the dimensionality of the theory. There exists a number of ways to avoid the doubling problem, but all of them break chiral invariance in one way or the other, an inevitable fact encoded in the Nielsen-Ninomiya theorem.¹⁷ The solution we have chosen for our simulations of graphene is the “staggered” fermion representation of Ref. 18. This choice is optimal for the study of spontaneous chiral symmetry breaking in graphene, as it yields the correct number of degrees of freedom while also partially preserving the original chiral symmetry of the theory, as will be shown in this section.

In order to discretize the fermionic sector of Eq. (2.2) in a way amenable to computer simulations, there are a number of choices that need to be made. As a first step, the fermions are integrated out, and the problem is formulated using the partition function written purely in terms of the gauge field [Eq. (2.16)]. The fermions are then represented exclusively through the determinant of the Dirac operator D . One can attempt to compute the determinant exactly for a given θ configuration, which is feasible due to the low dimensionality of the problem, and is what we have done for part of our calculations. Alternatively one may use the so-called pseudo-fermion method, which we will briefly explain in Sec. IV.

In order to arrive at the staggered fermion formulation, a useful starting point is the “naïvely” discretized action,

$$S_E^f[\bar{\psi}, \psi, \theta] = - \sum_{\mathbf{n}, \mathbf{m}} \bar{\psi}_{b,\mathbf{n}} D_{\mathbf{n},\mathbf{m}}[\theta] \psi_{b,\mathbf{m}}, \quad (3.12)$$

where

$$D_{\mathbf{n},\mathbf{m}}[\theta] = \frac{1}{2} \gamma_0 (\delta_{\mathbf{n}+\mathbf{e}_0,\mathbf{m}} U_{\mathbf{n}} - \delta_{\mathbf{n}-\mathbf{e}_0,\mathbf{m}} U_{\mathbf{m}}^\dagger) + \frac{v}{2} \sum_i \gamma_i (\delta_{\mathbf{n}+\mathbf{e}_i,\mathbf{m}} - \delta_{\mathbf{n}-\mathbf{e}_i,\mathbf{m}}) + m_0 \delta_{\mathbf{n},\mathbf{m}}, \quad (3.13)$$

with $U_{\mathbf{n}} = \exp(i\theta_{\mathbf{n}})$. It should be noted that for small m_0 , Eq. (3.13) becomes ill-conditioned, such that the “chiral limit” $m_0 \rightarrow 0$ has to be reached by extrapolation. The boundary conditions of the fermion fields are periodic in the spatial directions and antiperiodic in the temporal direction. It is possible, using a local unitary transformation on the fermion fields, to simultaneously diagonalize the Dirac matrices in Eq. (3.13) and thereby decouple the spinor components. This procedure, known as the Kawamoto-Smit transformation¹⁹ or simply as “spin-diagonalization,” is defined by

$$\begin{aligned} \psi_{\mathbf{n}} &\rightarrow T_{\mathbf{n}} \chi_{\mathbf{n}}, \\ \bar{\psi}_{\mathbf{n}} &\rightarrow \bar{\chi}_{\mathbf{n}} T_{\mathbf{n}}^\dagger, \end{aligned} \quad (3.14)$$

which in the Dirac operator (3.13) effects the transformation

$$\gamma^\mu \rightarrow T_{\mathbf{n}}^\dagger \gamma^\mu T_{\mathbf{n}+\mathbf{e}_\mu}, \quad (3.15)$$

on the Dirac matrices γ^μ . The transformed fermion fields $\chi_{\mathbf{n}}$ are referred to as staggered spinors. It is straightforward to show that the choice $T_{\mathbf{n}} = \gamma_0^{n_0} \gamma_1^{n_1} \gamma_2^{n_2}$ satisfies

$$T_{\mathbf{n}}^\dagger \gamma^\mu T_{\mathbf{n}+\mathbf{e}_\mu} = \eta_{\mathbf{n}}^\mu, \quad (3.16)$$

where the Kawamoto-Smit phases are given by

$$\begin{aligned} \eta_{\mathbf{n}}^0 &= 1, \\ \eta_{\mathbf{n}}^1 &= (-1)^{n_0}, \\ \eta_{\mathbf{n}}^2 &= (-1)^{n_0+n_1}. \end{aligned} \quad (3.17)$$

In this fashion the Dirac structure is removed, resulting in a sum of four identical terms in the action, one for each component of the original four-component Dirac spinor $\psi_{\mathbf{n}}$. These copies are referred to as staggered flavors. It has been shown in Ref. 20 that for each staggered flavor one recovers, in the continuum limit, two four-component Dirac flavors. Thus, by retaining one staggered flavor, it is possible to have exactly eight continuum fermionic degrees of freedom, which is the correct number for graphene. The action of a single staggered flavor is given by

$$S_{EL}^f[\bar{\chi}, \chi, \theta] = - \sum_{\mathbf{n}, \mathbf{m}} \bar{\chi}_{\mathbf{n}} K_{\mathbf{n}, \mathbf{m}}[\theta] \chi_{\mathbf{m}}, \quad (3.18)$$

where the staggered Dirac operator is

$$\begin{aligned} K_{\mathbf{n}, \mathbf{m}}[\theta] &= \frac{1}{2} (\delta_{\mathbf{n}+\mathbf{e}_0, \mathbf{m}} U_{\mathbf{n}} - \delta_{\mathbf{n}-\mathbf{e}_0, \mathbf{m}} U_{\mathbf{m}}^\dagger) \\ &+ \frac{v}{2} \sum_i \eta_{\mathbf{n}}^i (\delta_{\mathbf{n}+\mathbf{e}_i, \mathbf{m}} - \delta_{\mathbf{n}-\mathbf{e}_i, \mathbf{m}}) + m_0 \delta_{\mathbf{n}, \mathbf{m}}. \end{aligned} \quad (3.19)$$

The operator K thus replaces D in all expressions for the probability, chiral condensate, and susceptibility that were derived in Sec. II. As expected from the Nielsen-Ninomiya theorem, the staggered lattice action does not retain the full $U(4)$ chiral symmetry of the original graphene action at finite lattice spacing. As shown in Ref. 20, only a subgroup $U(1) \times U(1)$ remains upon discretization. Spontaneous condensation of $\bar{\chi}\chi$, or equivalently the introduction of a parity invariant-mass term, reduces this symmetry to $U(1)$. The focus of this work is on the phase transition associated with such a chiral symmetry-breaking pattern.

Finally, it should be pointed out that the situation concerning graphene is unusually favorable, in the sense that the staggered formalism somewhat fortuitously provides the correct number of fermionic degrees of freedom as $N_f=2$ for graphene monolayers. In general, staggered fermions provide only a compromise solution in the sense that some degree of chiral symmetry is preserved, at the price of retaining some of the doubling originally present in the discretized fermion action. Indeed, if the case of $N_f=1$ were to be simulated, it would be necessary to resort to the uncontrolled and contro-

versial ‘‘rooting’’ trick,²¹ whereby the desired number of continuum flavors is restored by taking the appropriate root of the Dirac operator.

C. Computation of observables

The computation of σ and χ_l from ensembles of gauge-field configurations necessitates, in principle, the full inversion of K and K^2 . Such a procedure may potentially become extremely time consuming for large lattices. In this respect, a choice exists between direct sparse solvers, such as PARDISO,²² and iterative solvers of the conjugate gradient type, such as BICGSTAB.²³ As the lattice size is increased, the performance of the direct solver scales much worse than the iterative solver, by a factor roughly proportional to the lattice volume. Nevertheless, the direct sparse solvers remain an attractive choice for a number of reasons: the performance of a direct solver is independent of the condition number of K , which is the ratio of its largest and smallest eigenvalues, and this is particularly significant close to a transition and for small m_0 . Furthermore, direct solvers feature optimized parallelization and are efficient at handling inversion problems with multiple right-hand sides. In view of this, PARDISO has been found to be the solver of choice for the efficient computation of observables on the presently used lattice volumes.

Regardless of the type of solver used, the full inversion of K quickly becomes impractically expensive when the lattice size is increased. In this situation, it is possible to resort to a stochastic estimator,²⁴ which constitutes an alternative to the exact calculation of $\text{Tr}(K^{-1})$. A suitable stochastic estimator for σ is given by

$$\hat{\sigma} = \frac{1}{V} \sum_{\mathbf{n}, \mathbf{m}} \xi_{\mathbf{n}}^\dagger K_{\mathbf{n}, \mathbf{m}}^{-1}[\theta] \xi_{\mathbf{m}}, \quad (3.20)$$

where the $\xi_{\mathbf{n}}$ are random Gaussian variables which satisfy $\langle\langle \xi_{\mathbf{n}} \rangle\rangle = 0$ and $\langle\langle \xi_{\mathbf{m}}^\dagger \xi_{\mathbf{n}} \rangle\rangle = \delta_{\mathbf{m}, \mathbf{n}}$, where the double bracket notation indicates an average over $\xi_{\mathbf{n}}$.

For a given gauge configuration, averaging Eq. (3.20) over $\xi_{\mathbf{n}}$ yields $\text{Tr}(K^{-1})$, which only requires application of the inverse to a limited number of random Gaussian vectors. With this approach it is also straightforward to compute $\text{Tr}(K^{-2})$, by simply applying the inverse to each random vector one more time. Adequate accuracy for σ and χ_l is achieved using ~ 100 random vectors for each gauge configuration, independently of the lattice volume used.

IV. MONTE CARLO STRATEGIES

This section presents the two Monte Carlo algorithms that we have used to study the discretized low-energy effective theory of graphene. We begin by outlining the Metropolis Monte Carlo algorithm which, although conceptually simpler, becomes computationally inefficient beyond a certain lattice volume, after which we proceed to describe the more advanced and highly efficient approach involving the Hybrid Monte Carlo (HMC) algorithm with pseudofermions.

A. Metropolis Monte Carlo

As shown in Sec. II B, the structure of the fermion determinant allows for a positive definite probability measure. Indeed, as shown in Sec. II C, an effective action can be defined such that expectation values of observables can be written as averages over field configurations weighted by

$$P[\theta] \equiv \exp(-S_{\text{eff}}[\theta]) = \det(K[\theta]) \exp(-S_E^g[\theta]), \quad (4.1)$$

where the matrix K corresponds to the staggered Dirac operator of Eq. (3.19). In the Metropolis algorithm,²⁵ a given gauge-field configuration θ is updated by the introduction of a small change at a randomly chosen lattice site. The updated configuration θ' is then accepted with probability

$$p \equiv \frac{P[\theta']}{P[\theta]} = \exp(-\Delta S),$$

$$\Delta S = S_{\text{eff}}[\theta'] - S_{\text{eff}}[\theta]. \quad (4.2)$$

If the new configuration θ' is rejected, θ is retained, and a new change proposed. In this fashion, a so-called Markov chain of gauge configurations is generated, in which the samples are distributed according to the desired probability measure. After an appropriate number of thermalization steps, gauge configurations can be saved at regular intervals, which should allow for adequate decorrelation. The central limit theorem then guarantees that for \mathcal{N} uncorrelated samples, the statistical uncertainties will decrease as $1/\sqrt{\mathcal{N}}$. The decorrelation can be measured in terms of the number of full sweeps of the lattice required between two consecutive observations, in order for the autocorrelation of the ensemble of gauge configurations to become insignificant. For the Metropolis algorithm, a proper balance between update size and decorrelation is achieved for acceptance rates of $\sim 60\text{--}70\%$.

In spite of its simplicity, the Metropolis approach has several inherent disadvantages. The most serious one arises as the fermion action is nonlocal, in the sense that updating a single lattice site requires a full recalculation of $\det(K)$. This disadvantage is exacerbated by the fact that decorrelation is dependent on the number of full sweeps of the lattice, and the number of sites to be updated increases as the lattice size is increased. Even with highly efficient parallel sparse solvers, the execution time scales as $\sim V^3$, such that it is bound to become impractical above a certain maximum lattice size. Also, as the updates in the Metropolis algorithm are entirely random, it is usually only possible to update very few lattice sites at once without ruining the acceptance rate. In Sec. IV B, we give an overview of the HMC algorithm, which is designed to overcome these difficulties.

B. Hybrid Monte Carlo

The problem of efficient updating of the gauge field in theories with dynamical fermions has been addressed in Ref. 26 where the Hybrid Monte Carlo algorithm was introduced. In this approach, the gauge field is evolved deterministically along a molecular dynamics (MD) trajectory, such that the entire lattice is updated at once. Thus, the number of updates required for decorrelation within the HMC algorithm is dra-

atically reduced, although the number of MD trajectories required for decorrelation roughly equals the number of sweeps necessary in the Metropolis approach.

The basic idea of the HMC algorithm is to evolve a given initial configuration $\theta_{\mathbf{n}}$ in a fictitious time τ according to the classical equations of motion, with a Hamiltonian given by

$$H = \sum_{\mathbf{n}} \frac{\pi_{\mathbf{n}}^2}{2} + S_E[\theta], \quad (4.3)$$

where $S_E[\theta]$ is the Euclidean action to be sampled, and $\pi_{\mathbf{n}}$ is a momentum conjugate to $\theta_{\mathbf{n}}$. This momentum is introduced as an auxiliary field, with the sole purpose of defining the above dynamics. The field $\pi_{\mathbf{n}}$ is of no consequence to the path integral that defines the theory, as its contribution factors out completely. It has been shown in Ref. 26 that the procedure of classically evolving $(\theta_{\mathbf{n}}, \pi_{\mathbf{n}}) \rightarrow (\theta'_{\mathbf{n}}, \pi'_{\mathbf{n}})$ using the above Hamiltonian, and choosing the initial $\pi_{\mathbf{n}}$ from a random Gaussian distribution, produces a Markov chain of gauge-field configurations distributed according to the desired probability measure.

Because the MD evolution is in principle exact, a trajectory that is long enough should provide the desired decorrelation between consecutive samples, provided that the pseudofermion field is refreshed at regular intervals. Ideally, a 100% acceptance rate should thus be achievable. In practice, however, the MD evolution is implemented with a finite time step $\Delta\tau$, which introduces a systematic error. However, as long as the evolution remains reversible, the effects of that error on the distribution of gauge-field configurations can be eliminated by means of a Metropolis step, comparing the initial and final configurations after each MD evolution, where Eq. (4.3) plays the role of the effective action in Eq. (4.2).

While the HMC algorithm achieves very efficient updating of the gauge field, a potentially serious drawback is that the updating procedure requires (in principle) the full evaluation of K^{-1} which is computationally prohibitively expensive, even more so than $\det(K)$. Because of this, a number of methods have been developed that seek to circumvent the necessity of calculating K^{-1} . In one of these, the so-called R algorithm,²⁷ the inverse is approximated by a stochastic estimator which, however, introduces a systematic error due to the loss of reversibility. Arguably, the method of choice is the Φ -algorithm,²⁷ which reduces the MD evolution into a sparse operation by re-expressing the square of the fermion determinant as a path integral over complex scalar fields known as pseudofermions, while simultaneously maintaining the desirable features of the HMC approach.

C. Pseudofermions

As the pseudofermion method is explained in great detail elsewhere (for pedagogical reviews, see Refs. 15 and 28) we shall only concern ourselves with outlining the basic idea, which is based on the identity

$$\det(Q) \propto \int \mathcal{D}\phi^\dagger \mathcal{D}\phi \exp(-S_E^p), \quad (4.4)$$

where the constant of proportionality is of no consequence. Here, ϕ, ϕ^\dagger are pseudofermion fields (which are bosonic but nevertheless satisfy antiperiodic boundary conditions in the temporal direction), $Q \equiv K^\dagger K$ and the pseudofermion action is

$$S_E^p = \sum_{\mathbf{n}, \mathbf{m}} \phi_{\mathbf{n}}^\dagger Q_{\mathbf{n}, \mathbf{m}}^{-1}[\theta] \phi_{\mathbf{m}} = \sum_{\mathbf{n}} \xi_{\mathbf{n}}^\dagger \xi_{\mathbf{n}}, \quad (4.5)$$

where ξ follows a Gaussian distribution, related to the pseudofermion field by $\phi = K^\dagger \xi$.

In order to simulate graphene, one requires $\det(K)$, not $\det(Q) = \det(K^\dagger K)$. Thus, using the pseudofermions according to the above prescription effectively doubles the number of degrees of freedom. Fortunately, the staggered fermion action allows for an odd-even decomposition,²⁸ such that a single staggered flavor can be simulated. In the odd-even decomposition, the lattice is separated into sublattices of even and odd sites, according to the sign of $(-1)^{n_0+n_1+n_2}$. Thus, as the derivative operator connects odd (even) sites with even (odd) ones, while the mass term connects odd (even) sites with odd (even) ones, the following odd-even decomposed form results,

$$K = \begin{pmatrix} m_0 & K_{oe} \\ K_{eo} & m_0 \end{pmatrix}, \quad (4.6)$$

and therefore

$$Q = \begin{pmatrix} K_{eo}^\dagger K_{oe} + m_0^2 & 0 \\ 0 & K_{oe}^\dagger K_{eo} + m_0^2 \end{pmatrix}, \quad (4.7)$$

which, using the fact that $K_{oe}^\dagger = -K_{eo}$, has been factorized into blocks of even-even and odd-odd elements. As a consequence,

$$\det(Q) = \det(K_{eo}^\dagger K_{oe} + m_0^2)^2. \quad (4.8)$$

Thus, in order to recover $\det(K)$, it suffices to retain only the even-even (or odd-odd) block of Q . In practice, this is implemented simply by discarding either the odd (or even) elements of ϕ .

In the presence of pseudofermions, the MD Hamiltonian becomes

$$H = \sum_{\mathbf{n}} \frac{\pi_{\mathbf{n}}^2}{2} + S_E^g + S_E^p, \quad (4.9)$$

and the equations of motion are

$$\dot{\theta}_{\mathbf{n}} = \frac{\delta H}{\delta \pi_{\mathbf{n}}} = \pi_{\mathbf{n}}, \quad (4.10)$$

$$\dot{\pi}_{\mathbf{n}} = -\frac{\delta H}{\delta \theta_{\mathbf{n}}} \equiv F_{\mathbf{n}}^g + F_{\mathbf{n}}^p, \quad (4.11)$$

where the ‘‘force term’’ associated with the gauge action takes the form

$$\begin{aligned} F_{\mathbf{n}}^g &\equiv -\frac{\delta S_E^g}{\delta \theta_{\mathbf{n}}} = -\frac{1}{g^2} \sum_{j=1}^3 \Im(U_{\mathbf{n}} U_{\mathbf{n}+\mathbf{e}_j}^\dagger - U_{\mathbf{n}-\mathbf{e}_j} U_{\mathbf{n}}^\dagger) \\ &= -\frac{1}{g^2} \left[6\theta_{\mathbf{n}} - \sum_{j=1}^3 (\theta_{\mathbf{n}+\mathbf{e}_j} + \theta_{\mathbf{n}-\mathbf{e}_j}) \right] + \dots, \end{aligned} \quad (4.12)$$

where $\Im(x)$ is the imaginary part of x ; the second line in this equation corresponds to the compact formulation and the last line, obtained by expanding in powers of θ , shows the result for the noncompact case. The pseudofermion contribution is given by

$$F_{\mathbf{n}}^p = -\frac{\delta S_E^p}{\delta \theta_{\mathbf{n}}} = -\sum_{\mathbf{n}} \phi_{\mathbf{n}}^\dagger \frac{\delta Q^{-1}}{\delta \theta_{\mathbf{n}}} \phi = \sum_{\mathbf{n}} \phi_{\mathbf{n}}^\dagger Q^{-1} \frac{\delta Q}{\delta \theta_{\mathbf{n}}} Q^{-1} \phi. \quad (4.13)$$

The essence of the Φ algorithm is the treatment of ϕ as a constant background field throughout each MD trajectory. After each MD evolution, the pseudofermion field is refreshed using random Gaussian noise according to $\phi = K^\dagger \xi$. Computationally, the great advantage of this algorithm is that in each step $\Delta\tau$, the calculational effort is reduced to applying the inverse of $K^\dagger K$ to a single vector ϕ , which is significantly less expensive than computing the full inverse.

The numerical integration of the MD equations of motion requires a reversible method, and the usual choice is the leap-frog integration formula²⁶ which is also area preserving. The calculation of the pseudofermion force in Eq. (4.13) is preferentially accomplished using an iterative solver such as BICGSTAB,²³ in which case the algorithm scales roughly as $\sim V$. Nevertheless, in practical calculations the scaling is inevitably somewhat worse, as the truncation error of the leap-frog method tends to increase with increasing lattice size, necessitating a smaller time step $\Delta\tau$.

In the present study of the low-energy effective theory of graphene, we have used both the Metropolis and HMC algorithms, verifying that for any given set of parameters the results agree within statistical uncertainties. We now turn to a presentation of our simulation results.

V. RESULTS

In our simulations, the fermions live in a volume of extent $V \equiv L_x^2 \times L_t$, while the gauge bosons also propagate in the z direction of length L_z . Increasing L_z beyond 8 was found to have no discernible effects. The results will thus be referred to by the short-hand notation $L_x^2 \times L_t$. Also, the action (2.2) has been rescaled according to Eq. (2.4), such that $\beta \equiv v/g^2$ and $v=1$ in the staggered Dirac operator of Eq. (3.19). Our simulations have been performed at finite (but small) values of m_0 , such that the limit $m_0 \rightarrow 0$ is reached by extrapolation.

We have performed simulations on lattice sizes up to $20^2 \times 20$ using the Metropolis method and $28^2 \times 28$ using HMC. The former method scales roughly as V^3 and therefore quickly becomes uneconomical when the lattice volume is increased. However, an advantage of the Metropolis method

is that the speed of the algorithm is independent of the condition number of the staggered Dirac operator K , as the fermionic determinant is evaluated using a direct solver. In contrast, the HMC algorithm with pseudofermions scales roughly as $\sim V$, if used together with an iterative solver such as BICGSTAB.²³ However, the HMC algorithm then becomes sensitive to the condition number of K , such that obtaining data becomes more difficult at small bare fermion masses or close to the critical coupling. This problem can be somewhat alleviated using a direct solver such as PARDISO,²² but in that case the HMC algorithm scales roughly as $\sim V^2$.

Within the Metropolis approach, ~ 240 uncorrelated configurations were generated for each value of (β, m_0) . When using the HMC algorithm, a similar number of MD trajectories were generated for each data point. The optimal MD time step $\Delta\tau$ was found to be dependent on the values of β and m_0 . In order to simultaneously optimize the acceptance rate, decorrelation, and execution time, $\Delta\tau$ was adjusted in the range $[0.01, 0.03]$, while the number of steps N_τ was chosen randomly from a Poisson distribution such that the average MD trajectory length between updates of the pseudofermion field was $\bar{\tau} = N_\tau \Delta\tau = 2$. The choice of $\bar{\tau} \approx 2.5$ was found to give optimal decorrelation.

The HMC algorithm is the method of choice for lattices larger than $20^2 \times 20$. As a check on the HMC code, the data points for $16^2 \times 16$ computed using the Metropolis algorithm in Ref. 5 were recomputed using the HMC method, and found to agree within statistical uncertainties. In all cases, the uncertainties were estimated using the Jackknife method.²⁹

A. The semimetal-insulator transition

In order to determine the critical coupling β_c for spontaneous chiral symmetry breaking, we calculated the chiral condensate σ and susceptibility χ_I for β between 0.05 and 0.5, and for m_0 between 0.0025 and 0.020 (in lattice units). Figure 2 shows our data for lattice sizes $20^2 \times 20$ (upper panels) and $28^2 \times 28$ (lower panels).

The chiral condensate increases as β is decreased, more sharply so below $\beta \approx 0.1$. This behavior becomes more pronounced as m_0 is decreased, providing the first indication of a phase transition as the Coulomb coupling is increased. In turn, the susceptibility also grows sharply around $\beta \approx 0.1$. This feature tends to disappear for $m_0 > 0.010$ as the lattice volume is increased. Thus, in order to understand the properties of the transition, masses smaller than $m_0 \sim 0.010$ should be used in the simulation. This situation is similar to that encountered in quenched QED₄ (Ref. 30) where it was concluded that for the critical region to be reached, bare masses smaller than ~ 0.025 should be used. On the other hand, for the smallest mass of $m_0 = 0.0025$, the change in the susceptibility as a function of the lattice volume appears to be relatively mild for $\beta > 0.09$. The rise in the susceptibility is therefore likely to be a real feature, indicating that the critical region has been reached.

In spite of the compelling qualitative evidence presented above, the nature of the simulational study precludes the use of bare masses m_0 that are small enough so that the distortion

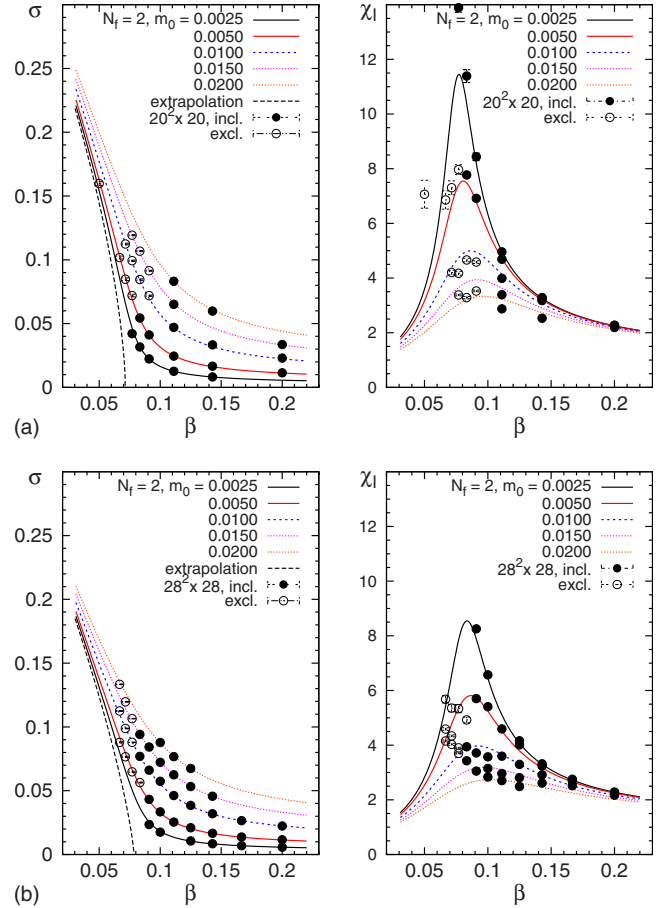


FIG. 2. (Color online) Chiral condensate (upper left panel) and susceptibility (upper right panel) for lattice size $20^2 \times 20$. Lower panels show the same quantities for $28^2 \times 28$. The lines represent χ^2 fits of Eq. (5.8) to σ only, with X_0, X_1, Y_1, δ and β_c as free parameters; the data points with largest finite-size effects have been excluded from the fit. The optimal parameter values are: for $20^2 \times 20$, $X_0 = 0.665 \pm 0.2$, $X_1 = -0.280 \pm 0.088$ and $Y_1 = -0.2869 \pm 0.090$, $\delta = 2.27 \pm 0.13$, $\beta_c = 0.0721 \pm 0.0006$; for $28^2 \times 28$, $X_0 = 0.3427 \pm 0.028$, $X_1 = -0.190 \pm 0.014$ and $Y_1 = -0.179 \pm 0.014$, $\delta = 2.309 \pm 0.037$, $\beta_c = 0.0785 \pm 0.0003$. The uncertainties are purely statistical.

introduced is negligible. What is needed is a controlled way of obtaining information about the massless limit, using the data at hand, taken at small but finite m_0 . A suitable observable is provided by the logarithmic derivative R (Ref. 31) of the chiral condensate with respect to m_0 ,

$$R \equiv \left. \frac{\partial \ln \sigma}{\partial \ln m_0} \right|_{\beta} = \frac{m_0}{\sigma} \left(\frac{\partial \sigma}{\partial m_0} \right) \bigg|_{\beta}, \quad (5.1)$$

which allows for a more precise determination of the critical coupling β_c , as well as for an estimate of the universal critical exponent δ [see Eq. (5.4)]. In the limit $m_0 \rightarrow 0$, $R \rightarrow 1$ in the chirally symmetric phase since $\sigma \propto m_0$; while at the critical coupling $\beta = \beta_c$, one expects $R \rightarrow 1/\delta$. Finally, R vanishes in the limit $m_0 \rightarrow 0$ in the spontaneously broken phase, where $\sigma \neq 0$ for $m_0 \rightarrow 0$. The data on R in Fig. 3 (right panel) indicate that chiral symmetry is spontaneously broken for

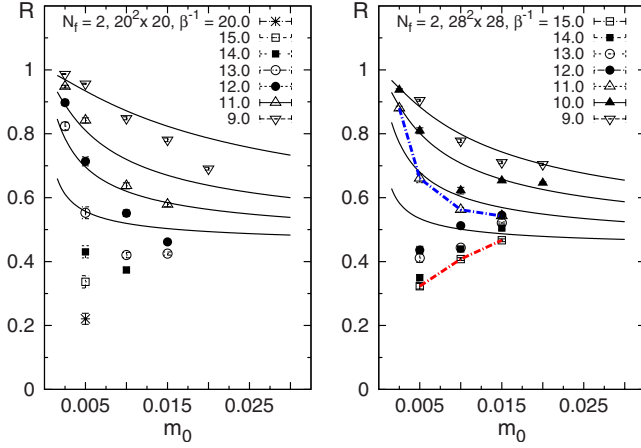


FIG. 3. (Color online) Logarithmic derivative R for lattice sizes $20^2 \times 20$ (left panel) and $28^2 \times 28$ (right panel). The solid lines for the largest four values of β correspond to the restricted fits shown in Fig. 2. The dashed red line in the right panel connects the data points for $\beta=1/15.0 \approx 0.067$, where the downward slope is characteristic of the spontaneously broken phase. On the other hand, the dashed blue line connecting the data points for $\beta=1/11.0 \approx 0.091$ clearly indicates that chiral symmetry remains unbroken in the limit $m_0 \rightarrow 0$ for that value of β . The evidence for spontaneous chiral symmetry breaking is significantly stronger for $28^2 \times 28$, where the data for $\beta=1/13.0 \approx 0.077$ are consistent with the broken phase, while for $20^2 \times 20$ the opposite is true. The $28^2 \times 28$ lattice favors a slightly larger value of β_c , while simultaneously disfavoring the classical critical exponent $\delta=3$.

$\beta=1/14.0 \approx 0.071$, but remains unbroken for $\beta=1/11.0 \approx 0.091$. We thus conclude, using the $28^2 \times 28$ data, that

$$0.071 < \beta_c < 0.091, \quad (5.2)$$

which could be further refined by use of larger lattice volumes and smaller values of m_0 .

B. Determination of the equation of state

While the logarithmic derivative R may provide model-independent information on the critical coupling as well as the exponent δ , it involves the chiral susceptibility and is therefore prone to large finite-size effects. A more accurate determination of β_c can be achieved by means of an appropriate equation of state (EOS)

$$m_0 = f(\sigma, \beta), \quad (5.3)$$

which is to be fitted to the simulation data on the chiral condensate. This EOS can then yield direct information on β_c as well as the critical exponents δ and $\bar{\beta}$, defined by

$$\delta \equiv \left[\frac{\partial \ln \sigma}{\partial \ln m_0} \right]^{-1} \Bigg|_{\beta=\beta_c, m_0 \rightarrow 0}, \quad (5.4)$$

$$\bar{\beta} \equiv \frac{\partial \ln \sigma}{\partial \ln(\beta_c - \beta)} \Bigg|_{m_0=0, \beta \nearrow \beta_c}. \quad (5.5)$$

In addition, using the scaling relation,

$$\bar{\beta}(\delta - 1) = \gamma, \quad (5.6)$$

one can obtain the critical exponent γ , defined by

$$\gamma \equiv - \frac{\partial \ln \chi}{\partial \ln(\beta_c - \beta)} \Bigg|_{m_0=0, \beta \rightarrow \beta_c}. \quad (5.7)$$

The EOS also provides a means for an extrapolation $m_0 \rightarrow 0$, which necessitates an *ansatz* for Eq. (5.3). We have considered an EOS similar to those successfully applied^{32–35} to QED₄,

$$m_0 X(\beta) = Y(\beta) f_1(\sigma) + f_3(\sigma), \quad (5.8)$$

where the functions X and Y are expanded around β_c such that $X(\beta) = X_0 + X_1(1 - \beta/\beta_c)$ and $Y(\beta) = Y_1(1 - \beta/\beta_c)$. The dependence of Eq. (5.8) on σ is

$$f_1(\sigma) = \sigma^b, \quad f_3(\sigma) = \sigma^\delta, \quad (5.9)$$

where $b \equiv \delta - 1/\bar{\beta}$. Thus Eq. (5.8) can be used to study deviations from the classical exponents $\delta=3$ and $\bar{\beta}=1/2$. It should be noted that for the case of QED₄,^{32–35} an extended version of the *ansatz* [Eq. (5.9)] has been used to include logarithmic corrections to the EOS.

While it is possible to fit both σ and χ_l simultaneously, it is advantageous to use the latter quantity as a consistency check only, as the finite-size effects are much smaller for σ . It is also useful to restrict the fit range to the data points where such effects are not too large. The results of the fits with restricted range are given in Fig. 2, whereas the results of a full fit to all data points are shown in Fig. 4. The results for β_c and δ are much more consistent for the restricted data set. The fit results for the restricted $28^2 \times 28$ data set indicate a critical coupling of $\beta_c = 0.0785 \pm 0.0003$ and a critical exponent $\delta = 2.309 \pm 0.037$. All of the fits described above have been performed using the constraint $b=1$, which is equivalent to the assumption $\gamma=1$, using Eq. (5.6). However, we have also relaxed this constraint by treating b as an additional free parameter in the fit. In all cases, no significant deviations from $b=1$ were found for any of the fits. Nevertheless, it would still be desirable to use larger lattices in order to minimize the finite-size effects at smaller values of β .

However, it is significant that the present results for both $20^2 \times 20$ and $28^2 \times 28$ favor values of $\delta \sim 2.3$ and $b \sim 1.0$, which strongly disfavors the classical mean-field exponents $\delta=3$, $\bar{\beta}=1/2$. Fits using classical exponents tend to become less and less favored when the lattice volume is increased, which is also reflected in the “Fisher plot” shown in Fig. 5. In particular, consistent fits for δ can be achieved using data for $20^2 \times 20$ and $28^2 \times 28$ if the fit range is restricted to those data points where the finite-size effects are under reasonable control, as shown in Fig. 2.

It has been argued in Ref. 7 that the semimetal-insulator phase transition should present an essential singularity, in the sense that the EOS for zero mass in the broken phase would be given by

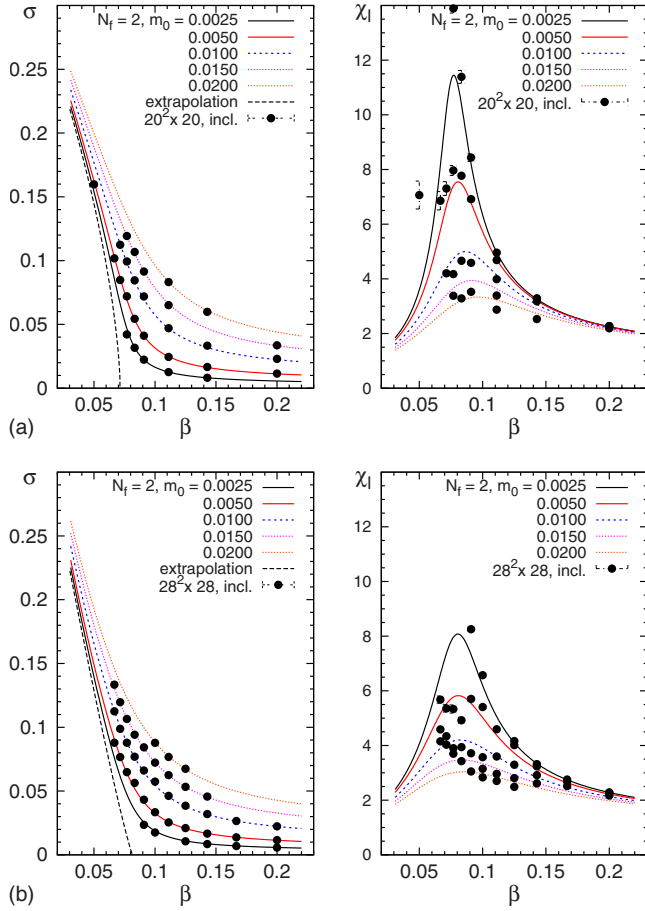


FIG. 4. (Color online) Chiral condensate (upper left panel) and susceptibility (upper right panel) for lattice size 20×20 . Lower panels show the same quantities for 28×28 . The lines represent χ^2 fits of Eq. (5.8) to σ only, with X_0, X_1, Y_1, δ and β_c as free parameters; all data points have been included in the fit, regardless of the estimated magnitude of finite-size effects. The optimal parameter values are: for $20^2 \times 20$, $X_0 = 0.364 \pm 0.029$, $X_1 = -0.156 \pm 0.013$ and $Y_1 = -0.159 \pm 0.013$, $\delta = 2.573 \pm 0.041$, $\beta_c = 0.0715 \pm 0.0003$; for $28^2 \times 28$, $X_0 = 0.834 \pm 0.024$, $X_1 = -0.409 \pm 0.011$ and $Y_1 = -0.418 \pm 0.012$, $\delta = 1.889 \pm 0.017$, $\beta_c = 0.0815 \pm 0.0004$.

$$\sigma = C_0 \exp\left(-\frac{C_1}{\sqrt{\beta_c - \beta}}\right), \quad (5.10)$$

with C_0, C_1 constants. This expression has vanishing derivatives to all orders at the critical point, and is said to be characterized by Miransky scaling.⁷ The critical exponents corresponding to such a transition are $\delta=1$, $\bar{\beta}=\infty$, and $\gamma=1$. This type of transition has sometimes been referred to as a Kosterlitz-Thouless transition, even though strictly speaking the latter does not involve spontaneous symmetry breaking. The value $\delta=1$ is apparently ruled out by the considerable dependence of the susceptibility on m_0 even for large values of β , which are far from the transition and where the finite-size effects are small. If the value of δ was close to unity, one would observe a susceptibility which is independent of m_0 as the critical point is approached. While our data does not favor an interpretation in terms of Miransky scaling, a full

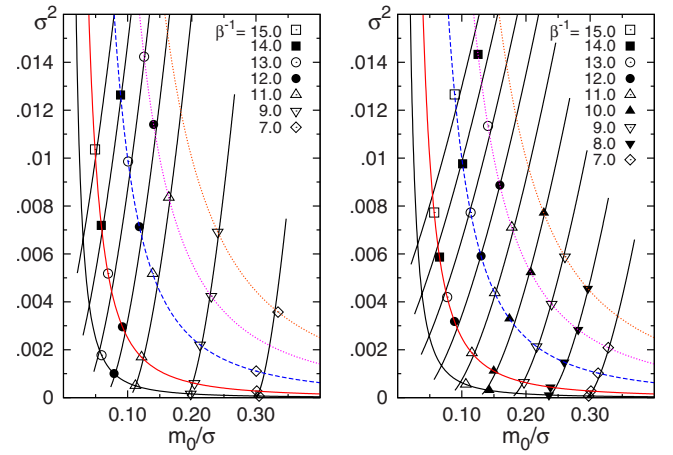


FIG. 5. (Color online) Fisher plot for lattice sizes of $20^2 \times 20$ (left panel) and $28^2 \times 28$ (right panel). The curved lines connect data points of equal m_0 , from the lower left-hand corner these are $m_0 = 0.0025, 0.005, 0.010, 0.015,$ and 0.020 . The vertical lines of equal β correspond to the restricted EOS fits shown in Fig. 2. The curvature in these lines indicates deviation from the classical critical exponents. At the critical coupling, the extrapolation of the lines of equal β crosses the origin. Finite-size effects tend to turn the lines clockwise.

consideration of this issue is beyond the scope of the present paper.

C. Finite-size effects

If a realistic picture of the properties of the semimetal-insulator transition, as exhibited by the low-energy effective theory considered here, is to be obtained, a proper assessment of the finite-size effects has to be made. In general, the lattice volume should ideally be large enough such that all explicit degrees of freedom (represented in this case by m_0) as well as any dynamically generated ones (the Goldstone boson associated with spontaneous chiral symmetry breaking) can be contained. In order to illustrate the finite-size effects, the chiral condensate and susceptibility have been plotted for volumes of $20^2 \times 20$ and $28^2 \times 28$ in Fig. 6.

As expected from the quite different nature of the low-energy theory of graphene in the spatial and temporal directions, the finite-size effects observed in the simulation are also different. Increasing the extent of the temporal dimension leads to an increase in the condensate σ , as would be expected by comparison with QED_4 where the finite-size effects are dominated by such behavior. The finite-size effects in the temporal dimension grow as m_0 is decreased, and do not depend strongly on β . This indicates that the effects are due to distortion of the staggered propagator involving the bare mass m_0 .

On the other hand, increasing the extent L_x of the spatial directions has a quite different effect on the chiral condensate. The effect is to lower the value of σ , which is opposite to the effect of increasing L_t . The relative change in σ also appears to be roughly independent of m_0 , such that the absolute shift is larger for larger values of m_0 . It is also noteworthy that the finite-size effects in L_x are very small in the

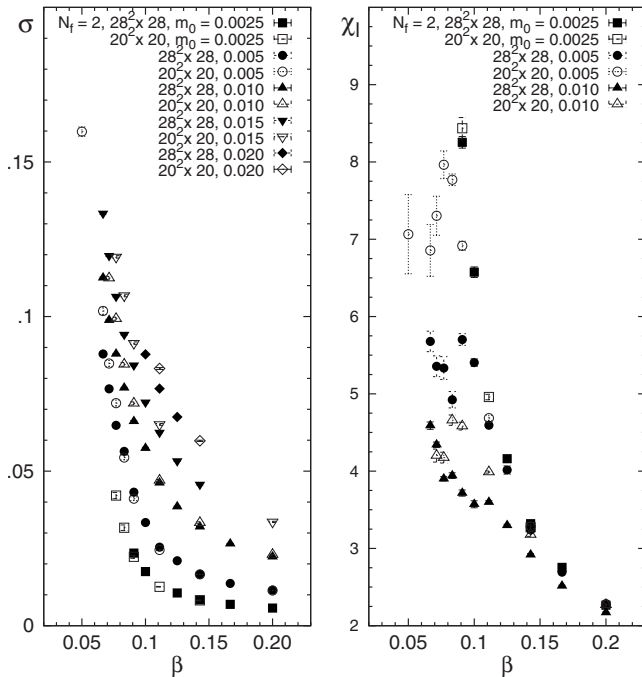


FIG. 6. Chiral condensate (left panel) and susceptibility (right panel), shown here for lattices sizes $20^2 \times 20$ (open symbols) and $28^2 \times 28$ (filled symbols). The finite-size effects are typically much larger for the susceptibility, and become large for the condensate as well at small β , particularly in the broken phase. Errors shown are purely statistical, and are in most cases comparable to the size of the data points.

unbroken phase, as shown in Fig. 6, while they quickly become large with the onset of spontaneous chiral symmetry breaking. We therefore conclude that these effects are due to the emergence of a dynamically generated Goldstone mode which is highly spatially extended.

For all the results presented here, the extent $L_z=8$ has been used for the bulk dimension, in which the fermionic degrees of freedom do not propagate. Increasing the size of that dimension has apparently no effect whatsoever on the results for the chiral condensate and susceptibility, as demonstrated by a comparison between results on a $14^2 \times 14$ lattice with $L_z=8$ and $L_z=14$. The results for all observables in question are compatible within statistical uncertainties, and binning of the data for σ into a histogram plot also shows no perceptible differences between the two event distributions. Apparently, restricting the bulk dimension to $L_z=8$ has no significant effect on the accuracy of our results, although an increased L_z can be accommodated if necessary, as this has little effect on the total computational cost. Such a result is nevertheless somewhat intuitive, as the fermions do not propagate in the bulk, and thus should be mostly insensitive to the presence of a boundary in that dimension. However, it should still be noted that^{32–34} in the context of QED₄ the main effect of the boundary is to introduce a constant background component into the gauge fields. In other words, at finite volume the results can be well described in terms of a renormalized staggered lattice propagator, augmented by a constant background field that may vary from one configuration to the next.

In addition to shifting the calculated values of the condensate, finite-size effects may also influence the distribution of the measured MC samples. We have observed that for small lattice volumes, the simulation exhibits a tendency to jump between two different states, akin to the effect noted in the QCD simulations of Ref. 24. This effect appears to be strongest in the quenched case, and weakens as more fermion flavors are added. The area of parameter space most affected is just above β_c , where the Coulomb interaction is not yet quite strong enough to break the chiral symmetry, and σ is strongly fluctuating. As this first-order feature also tends to disappear with increasing decorrelation and decreasing finite-size effects, we attribute it to a combination of these factors. This is in line with Ref. 24, where attempts to fit the event distribution with two Gaussians did not turn out satisfactorily.

VI. TESTS AND CROSS-CHECKS

In this section, we briefly describe the various tests performed in order to validate our simulations. Using the formalism described in Sec. III, we extended our code to perform simulations of QED in 2+1 dimensions (QED₃), and compared our results with those from Ref. 30. In this case the differences with graphene are that the gauge field lives in one less spatial dimension, and that all the components of the gauge field are dynamical, since Lorentz invariance is respected.

We have also developed another test based on QED in 3+1 dimensions (QED₄), which we compared with the results of Ref. 32–34. In this case the differences with graphene affect the fermion field, which lives in one more dimension. As in the previous case all the components of the gauge field contribute, as the theory is Lorentz invariant. Our lattice Monte Carlo implementation has satisfactorily passed all of the above mentioned tests. A comparison between our results for QED₃ and those of Ref. 30 is shown in Fig. 7.

In addition to these major checks, the following usually overlooked ones were also performed: explicit verification using a computer algebra system (CAS) of the correct structure of the staggered fermion operator, invariance of the action and the observables under gauge transformations, and reversibility of the HMC algorithm within each MD evolution. We finally note that the computing time required by the present calculations is $\sim 10^5$ CPU hours, which is in line with an estimate given by Hands and Strouthos in Ref. 10. Allocations of this size are routinely available at various supercomputing centers.

VII. OBSERVATION OF THE TRANSITION

The experimental detection of excitonic instabilities in graphene depends on the size of the induced gap Δ . Unfortunately, computing Δ in absolute units requires knowledge of a suitable dimensionful observable (other than Δ itself) to calibrate the calculation. To our knowledge such a quantity is not yet available. In Ref. 6, the excitonic gap was estimated within a gap-equation approach by assuming a value of the cutoff of the order of the inverse lattice constant of the

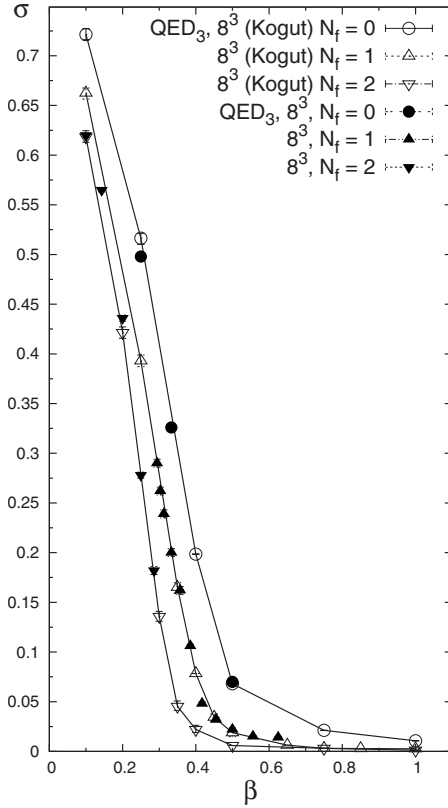


FIG. 7. Data of Ref. 30 compared with our implementation of the QED₃ simulation. The filled data points are our results, whereas the empty ones denote the results of Ref. 30. The lines connecting the data points of Ref. 30 are intended as a guide to the eye.

graphene honeycomb lattice. In that study, the gap was found to be of the order of a few tens of Kelvin. However, such a procedure only constitutes an order-of-magnitude estimate. As in our approach, the size of the gap can be determined in absolute units only after calibration of the calculation using a dimensionful observable.

Another issue of significance from the experimental point of view is the effect of impurities and lattice defects. These were investigated in Ref. 36, and they were found to have a substantial impact on the low-energy excitations in graphene. Also, Ref. 37 has studied the stability of the excitonic insulating phase in the presence of impurities, lattice defects and thermal fluctuations, and concluded that all of these effects tend to suppress the excitonic instability. Clearly, the experimental demonstration of the semimetal-insulator transition in graphene will be challenging from the point of view of sample quality.

As the mere presence of a substrate will likely eliminate the insulating phase due to screening of the Coulomb interaction, the most favorable experimental setup would involve samples of suspended graphene. Fortunately, this may also serve to eliminate most of the above mentioned concerns. Indeed, it has recently been found in Ref. 3 that in order to access the intrinsic electronic properties of graphene, thorough current annealing of suspended samples is necessary. The annealed samples were found to exhibit a greatly improved carrier mobility, far in excess of the values reported

for conventional samples on a substrate. Also, the demonstration of Shubnikov–de Haas (SdH) oscillations suggests that the mean-free path in current state-of-the-art suspended graphene is comparable to presently achievable sample dimensions of a few micrometers. Thus, graphene samples of sufficient quality to demonstrate the excitonic instability will likely be available in the near future.

To summarize, our work in Ref. 5 indicates that the excitonic insulating effect in graphene is unlikely to be observed unless the graphene sheet is freely suspended, such that the Coulomb interaction is not screened by the dielectric substrate. Further, the experimental work in Ref. 3 has demonstrated that the elimination of impurities and defects is necessary in order to access the intrinsic electronic properties of graphene. As both of these conditions can nowadays be fulfilled by experiment, we hope that the appearance of the excitonic gap will be demonstrated in the near future.

VIII. CONCLUSIONS

We have described the low-energy effective theory of graphene, its gauge and global symmetries, and shown how a discretized lattice formulation can be constructed such that it contains the correct number of degrees of freedom and partially retains chiral invariance at finite lattice spacing. We have also explained in detail the numerical methods employed to perform lattice Monte Carlo simulations of the discretized theory, focusing on the determination of the location and properties of the semimetal-insulator phase transition.

On the theoretical side, we conclude that our extended analysis is consistent with the findings of Ref. 5, which predict that suspended graphene should possess an excitonic gap in the band structure. We have now, using the HMC algorithm, extended the results of Ref. 5 to much larger lattice volumes, as well as smaller fermion masses. While the scenario first reported in Ref. 5 is confirmed by the present results, the larger lattices used also provide tantalizing hints that the phase transition is not of infinite order, as predicted in Ref. 7, nor is it likely to be described by classical critical exponents. In order to achieve a precise determination of the critical exponents it is necessary to perform simulations at much larger lattices, potentially as large as $48^2 \times 48$. We are currently exploring the feasibility of such simulations by benchmarking our code on a $36^2 \times 36$ lattice.

An accurate determination of the critical coupling and the critical exponents will provide a solid understanding of the universality class of this transition, as well as another piece of experimentally verifiable information on the electronic properties of graphene.

ACKNOWLEDGMENTS

We thank A. Andreev, W. Detmold, M. M. Forbes, R. J. Furnstahl, D. Gazit, Y. Nishida, and D. T. Son for instructive discussions and encouragement, and A. Bulgac and M.

Savage for providing computing time at the University of Washington. We also acknowledge helpful comments by V. Miransky and Ph. de Forcrand. This work was supported in part by an allocation of computing time from the Ohio

Supercomputer Center, by the National Science Foundation under Grant No. PHY-0653312 and U.S. DOE Grants No. DE-FC02-07ER41457 (UNEDF SciDAC Collaboration) and No. DE-FG-02-97ER41014.

-
- ¹K. S. Novoselov, *Science* **306**, 666 (2004); K. S. Novoselov, D. Jiang, T. Booth, V. V. Khotkevich, S. M. Morozov, and A. K. Geim, *Proc. Natl. Acad. Sci. U.S.A.* **102**, 10451 (2005); *Nature (London)* **438**, 197 (2005); A. K. Geim and K. S. Novoselov, *Nature Mater.* **6**, 183 (2007).
- ²A. H. Castro Neto, F. Guinea, N. M. R. Peres, K. S. Novoselov, and A. K. Geim, *Rev. Mod. Phys.* **81**, 109 (2009).
- ³K. I. Bolotin, K. J. Sikes, Z. Jiang, M. Klima, G. Fudenberg, J. Hone, P. Kim, and H. L. Stormer, *Solid State Commun.* **146**, 351 (2008); K. I. Bolotin, K. J. Sikes, J. Hone, H. L. Stormer, and P. Kim, *Phys. Rev. Lett.* **101**, 096802 (2008); V. Crespi, *Physics* **1**, 15 (2008); J. C. Meyer, A. K. Geim, M. I. Katsnelson, K. S. Novoselov, T. J. Booth, and S. Roth, *Nature (London)* **446**, 60 (2007); J. S. Bunch, A. M. van der Zande, S. S. Verbridge, I. W. Frank, D. M. Tanenbaum, J. M. Parpia, H. G. Craighead, and P. L. McEuen, *Science* **315**, 490 (2007).
- ⁴G. W. Semenoff, *Phys. Rev. Lett.* **53**, 2449 (1984).
- ⁵J. E. Drut and T. A. Lähde, *Phys. Rev. Lett.* **102**, 026802 (2009).
- ⁶D. V. Khveshchenko and H. Leal, *Nucl. Phys. B* **687**, 323 (2004); D. V. Khveshchenko, *Phys. Rev. Lett.* **87**, 246802 (2001).
- ⁷E. V. Gorbar, V. P. Gusynin, V. A. Miransky, and I. A. Shovkovy, *Phys. Rev. B* **66**, 045108 (2002).
- ⁸J. Gonzalez, F. Guinea, and M. A. H. Vozmediano, *Nucl. Phys. B* **424**, 595 (1994); *Phys. Rev. Lett.* **77**, 3589 (1996); *Phys. Rev. B* **59**, R2474 (1999).
- ⁹I. F. Herbut, *Phys. Rev. Lett.* **97**, 146401 (2006).
- ¹⁰S. J. Hands and C. G. Strouthos, *Phys. Rev. B* **78**, 165423 (2008).
- ¹¹P. R. Wallace, *Phys. Rev.* **71**, 622 (1947).
- ¹²S. Reich, J. Maultzsch, C. Thomsen, and P. Ordejón, *Phys. Rev. B* **66**, 035412 (2002).
- ¹³D. T. Son, *Phys. Rev. B* **75**, 235423 (2007).
- ¹⁴D. V. Khveshchenko, *J. Phys.: Condens. Matter* **21**, 075303 (2009).
- ¹⁵H. Rothe, *Lattice Gauge Theories*, 3rd ed. (World Scientific, Singapore, 2005).
- ¹⁶K. Farakos and G. Koutsoumbas, *Phys. Lett. B* **178**, 260 (1986); J. B. Kogut and C. G. Strouthos, *Phys. Rev. D* **71**, 094012 (2005).
- ¹⁷H. B. Nielsen and M. Ninomiya, *Nucl. Phys. B* **185**, 20 (1981); **195**, 541 (1982); **193**, 173 (1981).
- ¹⁸J. Kogut and L. Susskind, *Phys. Rev. D* **11**, 395 (1975); L. Susskind, *ibid.* **16**, 3031 (1977); H. Kluberg-Stern, *Nucl. Phys. B* **220**, 447 (1983).
- ¹⁹N. Kawamoto and J. Smit, *Nucl. Phys. B* **192**, 100 (1981).
- ²⁰C. Burden and A. N. Burkitt, *Europhys. Lett.* **3**, 545 (1987).
- ²¹M. Creutz, *Phys. Lett. B* **649**, 230 (2007).
- ²²O. Schenk and K. Gärtner, *FGCS, Future Gener. Comput. Syst.* **20**, 475 (2004); *Electron. Trans. Numer. Anal.* **23**, 158 (2006).
- ²³H. A. van der Vorst, *SIAM (Soc. Ind. Appl. Math.) J. Sci. Stat. Comput.* **13**, 631 (1992).
- ²⁴K. Bitar, A. D. Kennedy, R. Horsley, S. Meyer, and P. Rossi, *Nucl. Phys.* **313**, 348 (1989); **313**, 377 (1989).
- ²⁵N. Metropolis, A. W. Rosenbluth, M. N. Rosenbluth, A. H. Teller, and E. Teller, *J. Chem. Phys.* **21**, 1087 (1953).
- ²⁶S. Duane, A. D. Kennedy, B. J. Pendleton, and D. Roweth, *Phys. Lett. B* **195**, 216 (1987).
- ²⁷S. Gottlieb, W. Liu, D. Toussaint, R. L. Renken, and R. L. Sugar, *Phys. Rev. D* **35**, 2531 (1987).
- ²⁸T. DeGrand and C. DeTar, *Lattice Methods for Quantum Chromodynamics* (World Scientific, Singapore, 2006).
- ²⁹M. C. K. Yang and D. H. Robinson, *Understanding and Learning Science by Computer*, Series in Computer Science (World Scientific, Singapore, 1986), Vol. 4.
- ³⁰J. B. Kogut, E. Dagotto, and A. Kocić, *Phys. Rev. Lett.* **60**, 772 (1988); E. Dagotto, J. B. Kogut, and A. Kocić, *ibid.* **62**, 1083 (1989); S. J. Hands, J. B. Kogut, and C. G. Strouthos, *Nucl. Phys. B* **645**, 321 (2002).
- ³¹A. Kocić, J. B. Kogut, and K. C. Wang, *Nucl. Phys. B* **398**, 405 (1993).
- ³²M. Göckeler, R. Horsley, E. Laermann, P. E. L. Rakow, G. Schierholz, R. Sommer, and U. J. Wiese, *Nucl. Phys. B* **334**, 527 (1990).
- ³³M. Göckeler, R. Horsley, P. Rakow, G. Schierholz, and R. Sommer, *Nucl. Phys. B* **371**, 713 (1992).
- ³⁴M. Göckeler, R. Horsley, V. Linke, P. E. L. Rakow, G. Schierholz, and H. Stüben, *Nucl. Phys. B* **487**, 313 (1997).
- ³⁵A. A. Khan, *Phys. Rev. D* **53**, 6416 (1996).
- ³⁶V. M. Pereira, J. M. B. Lopes dos Santos, and A. H. Castro Neto, *Phys. Rev. B* **77**, 115109 (2008); A. La Magna, I. Deretzis, G. Forte, and R. Pucci, *ibid.* **78**, 153405 (2008).
- ³⁷G.-Z. Liu, W. Li, and G. Cheng, arXiv:0811.4471 (unpublished).